d-Electron tuned CoMoP for enhance 5-hydroxymethylfurfural oxidation and HER

Honglei Wang [a,*,1], Caiyun Niu [b,1], Wen Liu [a], Shengyang Tao [c,d,e,**]

[a] College of Chemical Engineering and Technology, Taiyuan University of Science and Technology, Taiyuan 030024, China
[b] School of Chemistry and Chemical Engineering, North University of China, Taiyuan 030051, China
[c] School of Chemistry, Dalian University of Technology, Dalian 116024, China
[d] State Key Laboratory of Fine Chemicals, Dalian University of Technology, Dalian 116024, China
[e] Frontier Science Center for Smart Materials Oriented Chemical Engineering, Dalian University of Technology, Dalian 116024, China

ARTICLE INFO

ABSTRACT

Implementing d-electron complementation by atomic doping can improve the catalyst's catalytic activity, but the exact active sites and detailed mechanism of this catalyst remain ambiguous in the oxidation of 5-hydroxymethylfurfural (HMFOR) and hydrogen evolution reactions (HER). Here, CoMoP nanoplates are successfully fabricated via the 3d orbital filling characteristics. It is found that Mo can disorder the coordination environment of Co, promoting surface electro-generation of MoO_x and CoOOH species. Meanwhile, CoP can only oxidize the formyl group to produce carboxylate, while MoO_x and CoOOH species are required to oxidize the hydroxyl group. Additionally, the introduction of Mo makes the lattice expansion of CoP leading to Co d-band center upshift, benefiting to hydrogen adsorption for enhancing HER activity. Therefore, selective production of 5-hydroxymethyl-2-furan carboxylic acid (HMFCA) and 2,5-furan dicarboxylic acid (FDCA) and promotion of HER reaction activity can be achieved through d-electron tuning.

1. Introduction

With the rapid increase in plastic product consumption, white pollution is becoming increasingly severe [1–3]. 2,5-furanedicarboxylic acid (FDCA) is considered a biomass-based monomer for sustainable polymer materials, which has a chemical structure similar to that of terephthalic acid, bisphenol A in plastic industrial products to reduce white environmental pollution [4–6]. Additionally, the polymer composed of FDCA possess furan structure, which exhibits more significant mechanical strength and gas barrier advantages, etc [7]. From dehydration of C-6 monosaccharides to prepare 5-hydroxymethylfurfural (HMF) and then to obtain FDCA have good application prospects [8, 9]. In the former research, the oxidation of HMF (HMFOR) to FDCA typically use harsh reaction conditions and precious metals, which increase production risks and costs [10–12]. Electrochemistry has the advantage of mild reaction conditions, which can provide a safe reaction path for HMFOR [13–15].

The performance index of the electrocatalyst is the bottleneck of improving the electrocatalytic reaction efficiency [16,17]. In most of the HER and HMFOR electrocatalysts, cobalt-based phosphides possess excellent catalytic activity because their bond moderately ability with reactant intermediates [18–20]. Nevertheless, their applications in electrocatalysis remain challenging due to unfavorable intrinsic electronic structures and unsatisfactory adsorption behaviors of active species [21]. Heteroatom doping has become one of the most effective methods to improve the intrinsic activity of HER and HMFOR [21–24]. Due to the heteroatoms can change the crystal environment of catalytic material and utilize the filling characteristics of d-orbitals, enhancing the active intermediate adsorption behavior, which improves the performance of catalytic materials [25–28]. Accordingly, we expect that the HER and HMFOR activity can be improved by using an ideal dopant to tune the electronic structure of the catalyst and enhance its adsorption behavior to active species.

Previous reports are considering that the 3d electrons in Co can fill the empty 3d orbitals in the oxidation state of Mo when they coexist in interstitial compounds [29,30]. We constructed

---

* Corresponding author.
** Corresponding author at: School of Chemistry, Dalian University of Technology, Dalian 116024, China.
E-mail addresses: wanghonglei89@tyust.edu.cn (H. Wang), taosy@dlut.edu.cn (S. Tao).
[1] Honglei Wang and Caiyun Niu contributed equally to this work.

molybdenum-incorporated cobalt phosphide as an electrocatalyst to promote HER and HMFOR activities. Introducing Mo can make the lattice expansion of CoP, which upshifts Co d-band center and decreases |ΔGH*| values for boosting HER activity. In situ Raman spectroelectrochemical results confirm that Mo promotes CoMoP surface electro-generation CoOOH and Mo-O species layer, which is the real active site for the initial oxidation of hydroxyl. Besides, the assembled continuous flow electrochemical reactor employing CoMoP as both electrodes drive HER and HMFOR requires 1.36 V potential and remarkable stability.

2. Experimental section

2.1. Materials

$(NH_4)_6Mo_7O_{24}\cdot4H_2O$, cobaltous nitrate hexahydrate (Co $(NO_3)_2\cdot6H_2O)$, sodium monophosphate $(NaH_2PO_2\cdot H_2O)$, NH_4F, HCl, urea, ethanol, chromatographic methanol and KOH were acquired to Kermel Reagent Factory. Furan compounds such as $C_6H_6O_3$ (HMF), $C_6H_4O_5$ (FDCA), $C_6H_4O_4$ (FFCA), $C_6H_6O_4$ (HMFCA) and $C_6H_4O_3$ (DFF) were acquired by Alfa Factory. Nickel materials were obtained by Baoji Zhiming Co., Ltd.

2.2. Production of CoMoP

CoMoP was fabricated from Mo-doping $Co(CO_3)_{0.5}OH\cdot0.11H_2O$ by the hydrothermal progress. In detail, 2 mM cobalt salt, (0.1 mM, 0.3 mM, 0.5 mM, 0.7 mM, 0.9 mM, and 1.1 mM) ammonium molybdate, 0.2 g $CO(NH_2)_2$, and 0.2 g NH_4F were dissolved with 0.045 L water. Then, the solution was placed in autoclave. After that, the autoclave was heated to 80 ºC and kept warm for 18 h. Afterwards, autoclave will stop heating and cool down. Next, Mo-doping Co-precursor was obtained. Afterward, the Mo-doping Co-precursor (cobalt salt: 0.7–1.1 mM) and NaH_2PO_2 powder were heated at 310 ºC for 2 h in inert gas. Then, gray CoMoP was prepared.

2.3. Production of CoP

The production of CoP is consistent with CoMoP, except that the Mo salt was not added when the Co-precursor was synthesized.

2.4. Production of flow-reactor

Employing the SolidWorks software to design the flow-reaction. Among them, flow-reactor was printed by an isun3d 230 C. Using photopolymer resin come from Polymaker Company as raw material for manufacturing flow-reactor. After that, flow-reactor was obtained by printing layer by layer for 2 h.

2.5. Structural testing and instruments

Using the TEM (JEM1011) and SEM (Phenom Pharos G2) to characterize morphological information of CoMoP and CoP. Utilizing XRD (Rigaku D/Max 2400), XPS (Shimadzu Krotas Amicus), Raman spectra (Thermo Fisher), and Infrared spectra (IS50) to characterize the structural information of CoMoP and CoP. XAFS characterization will be obtained to Shanghai Synchrotron Radiation Facility.

2.6. In situ spectroscopic characterization

Put the flow reaction cell of the three-electrode system connected with the working electrode CoMoP under the Raman spectrometer, and flow 100 mM HMF into the reaction cell through the peristaltic pump. Record the test results 20 s after the reaction begins, and test three times as a comparison.

2.7. Electrochemical measurements

Employing CHI660E electrochemical work station to test cyclic voltammetry (CV) curve, current time (I-T) curve and electrochemical impedance curve, etc. All electrochemical tests were performed with iR compensation, unless otherwise specified. The electrochemical double layer capacitance, conversion frequency, Faraday efficiency, resistance and overpotential under corresponding voltage of the sample were estimated through the corresponding test results. The electrochemical active surface area (ECSA) of all catalysts was estimated from the C_{dl} by diving the C_{dl} value by the specific capacitance (ECSA = C_{dl}/C_s, where a C_s value of 0.035 mF cm^{-2} was employed [31]). The current densities of the samples were normalized by the ECSA values according to the equation:

$$j_{ECSA} = \frac{j}{ECSA}$$

All electrochemical tests were calculated based on reversible hydrogen electrodes: RHE = E (Hg/HgO) + 0.098 V + 0.059 × pH. The turnover frequencies (s^{-1}) were calculated follow:

$$TOF = \frac{I}{2Fn}$$

where I is current (A) during polarization curve measurement. F is Faraday constant (C/mol). n is number of active sites (mol). 1/2 is based on the fact that forming a hydrogen molecule requires two electrons. The exchange current density is calculated based on the Tafel plot extrapolation method. The Tafel calculation formula is:

$$\eta = a + b\log j$$

where η is overpotential (V). j is current density. a and b are constant. The intercept of extrapolating the Tafel curve to an overpotential of 0 is $b\log j_0$, thereby the exchange current density j_0 is obtained by intercept and Tafel slope b.

2.8. HPLC analysis

Use high-performance liquid chromatography to detect reactants and products. The detectors for chromatography are UV visible detectors and C18 columns. The mobile phase is ammonium formate and methanol, the ratio is 7:3, the flow-rate is 1 mL/min, and the detector wavelength is 265 nm. The calculation formula for each substance is as follows:

$$HMF\ conversion\ (\%) = \frac{n\ (HMF\ consumed)}{n\ (initial\ HMF)} \times 100\ \% \qquad (1)$$

$$FDCA\ selectivity\ (\%) = \frac{n\ (FDCA\ formed)}{n\ (initial\ HMF)} \times 100\ \% \qquad (2)$$

$$Faradaic\ efficiency\ (\%) = \frac{n\ (FDCA\ formed)\ \times\ 6F}{total\ electricity\ passed} \times 100\ \% \qquad (3)$$

Among them, F is 96,485 C mol^{-1}.

2.9. Computational methods

Density functional theory (DFT) calculations will be used to obtain the electronic density of states and adsorption energy of the sample model. Enhanced wave potential was employed to explore the ion nucleus information. The model calculation results are determined to be convergent when the energy vary is below eV Å^{-1}. The calculation of material adsorption energy was obtained by the following formula:

$$Adsorption\ energy = Adsorbate/Substrate\ energy - Adsorbate\ energy - Substrate\ energy$$

2.10. Numerical simulation calculation

The computer software COMSOL Multiphysics 5.4 was used to simulate the flow electrochemical reactor in Multiphysics simulation under electric field and smooth conditions. The simulation conditions are secondary current distribution, laminar flow, three reactor components, reactant concentration (100 mM), and inlet flow rate set at 0.2 mL/min. The other set conditions are consistent with the laboratory and conditions.

3. Results and discussion

3.1. Physical characterization of CoMoP

CoMoP is grown on Ni foam by thermal phosphating from basic carbonate precursor following a well-established protocol (Scheme 1). Monitoring of prepared sample through scanning electron microscopy (SEM) pictures (Fig. 1a), we observe the interweaving growth CoMo-precursors nanoplates (molybdenum salts content: 1.1 mM) be fabricated on the surface of Ni Foam by hydrothermal. To explore the nanoplate formation progress, we monitored the effect of different cobalt and molybdenum salt ratios on surface morphology during the hydrothermal process. Precursor exhibits sea urchin-like structure when there is too little molybdenum salt in system, while hydrotalcite-like nanoplate structure is appeared with the increase of Mo salt content (Fig. S1).

Fig. 1b shows that the CoMo-precursor reacted with sodium hypophosphite monohydrate to obtain CoMoP (300°C). SEM data indicate the nanoplate morphology is well maintained after high-temperature reaction. This interlaced structure with nanoplates can increase the effective contact area between the catalyst and the reactants, promoting catalytic activity. The Co, Mo, P, and O elements are evenly distributed on the nanoplates, as observed by their corresponding color mappings (Fig. S2a). Fig. S2b and Table S1 show that the content of each element in CoMoP, which further confirms the successful introduction of Mo. Transmission electron microscope (TEM) indicates the sample is composed of nanoplate (Fig. 1c). In the high-resolution TEM (HRTEM) data, the sample possess both of the 2.35 and 1.19 Å lattice spacing, which is 0.02 Å increase compared to the CoP (201) and (211) lattice planes corresponding lattice spacing (Fig. 1d). This result indicates that Mo incorporation CoP causes lattice expansion. Mapping data suggests that each element in CoMoP is distributed on the nanoplate. (Fig. 1e). The atomic force microscopy is used to reveal the thickness of the CoMoP nanosheets. The test results show that the thickness of the nanosheets is 14.2 nm (Fig. S3).

X-ray diffraction (XRD) identifies the sample's crystal structure. Fig. 2a shows the diffraction peaks at $2\theta = 45°$, $52°$, and $76°$ match well with the Ni foam. Besides these peaks, the other peaks (31.7°, 36.5°, 46.3°, 48.2°, 52.6°, and 56.7°) are related to the (011), (111), (112), (211), (103), and (301) planes of CoP (PDF No. 29–0497), demonstrating that CoP is the principal phase for CoMoP. Significantly, the diffraction peak of CoMoP shifts negatively by 0.36° compared to CoP. The shift of diffraction.

peaks may be caused by lattice parameters adjusted by Mo atoms replacing part of Co atoms, which match the HRTEM test results. Employing the X-ray photoelectron spectroscopy spectra (XPS) explore the effect for incorporation Mo on the electron structure of CoP. As shown in Fig. 2b, the samples containing Co, Mo, P, and O elements, where O element stems from atmosphere. Co XPS spectra of CoMoP present three doublet peaks (Fig. 2c), which can be assigned to $CoMoO_4$ species (781.9/797.9 eV), Co-O species (783.6/799.5 eV), and satellite peaks (785.4/802.8 eV), respectively [32–34]. Compared to CoP, the Co 2p binding energy positive shift by ~0.4 eV, indicating that the embedded Mo atom can modify the electronic structure of Co centers.

Fig. 2d suggest that the Mo 3d peaks are related to Mo^{3+} (232.9/236.4 eV), Mo^{4+} (233.7 eV), and Mo^{6+} (235.8 eV), respectively [34–36]. The ionic radius of Mo in the valence of 4/6 is 0.68/0.65 Å [37, 38], slightly large than that of Co (0.55 Å) [39]. Therefore, Mo ion can easily be inserted into the lattice of CoP, leading to lattice expansion [40]. Fig. 2e shows the P 2p spectra. The peaks locate at 129.9, 130.7, and 134.4 eV are related to P 2p3/2, P 2p1/2, and P-O species (from superficial oxidation), respectively [41]. The weak intensity of P 2p peak may be due to the shallow detection depth of XPS and interference from surface oxide layers. Significantly, P binding energy negative shifts 0.1 eV relative to that of CoP, demonstrating the electrons transfer to P and accumulate around it after Mo incorporation [42]. The O1s spectra possess four different peaks (Fig. 2f), which correspond to lattice oxygen (Metal-O; 531.8 eV), metal-OH (532.3 eV), defects-O (533.5 eV), and adsorbed-O (534.1 eV), respectively [43].

To investigate the coordination information and geometric distribution of CoMoP, the synchrotron radiation X-ray absorption near edge structure (XANES) spectra were measured [44,45]. The result show that the Mo average valence state in CoMoP is higher than that of Mo foil and MoP (Fig. 2g, and inset). Fig. S4a shows that the Co average valence state in CoMoP is higher than that of Co foil and CoP. The above result shows that Mo incorporation leads to higher valence states for Mo and Co in CoMoP, which promotes the HMFOR because the high valence species can typically enhance the oxidation reaction [46,47]. Fig. S4b and Table S2 indicate the different periods and amplitudes of CoMoP by quantitative XAFS data. The coordination number of Mo-O, Mo-P, and
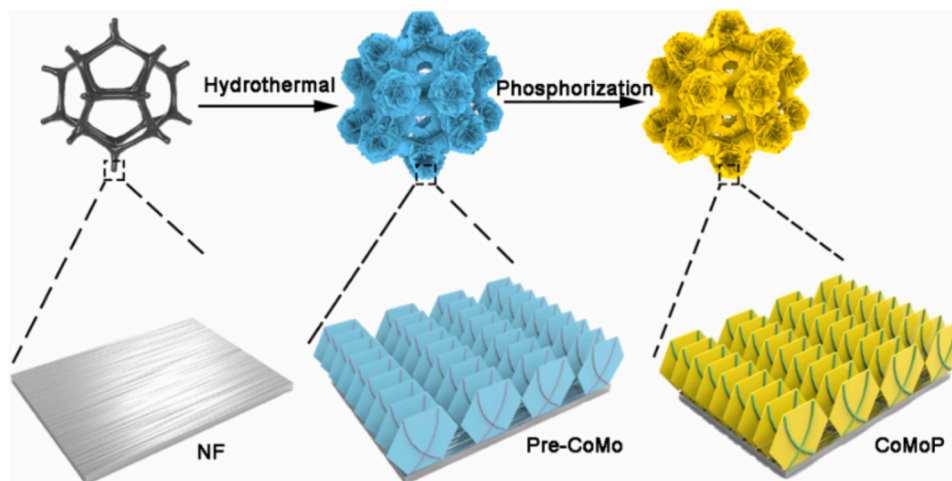
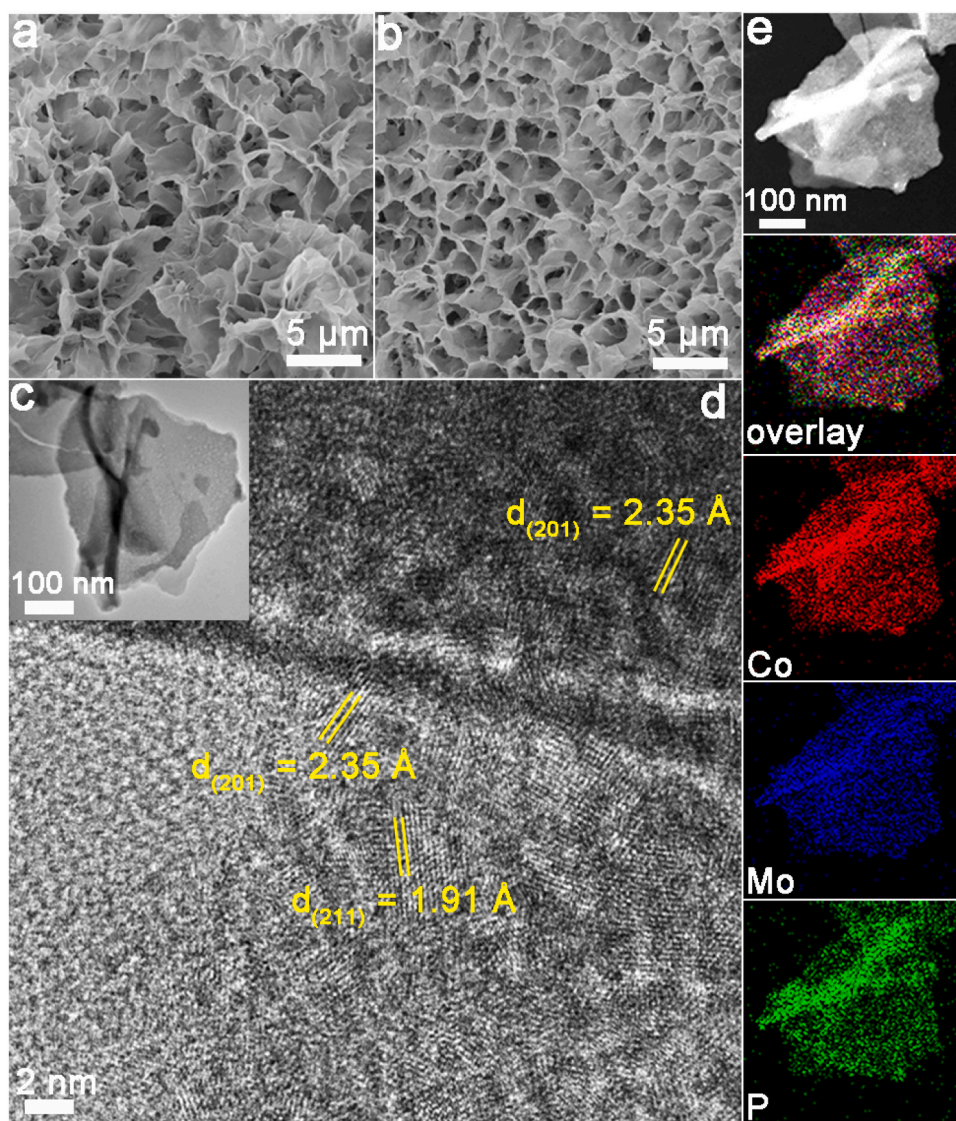**Scheme 1.** Schematic diagram of the synthesis of CoMoP.

Fig. 1. (a) SEM images of CoMo-precursors and (b) CoMoP. (c) TEM image, (d) HRTEM image, and (e) TEM elemental mapping images of CoMoP.

Mo-Co bonds matching 2.40, 2.86, and 3.31, respectively, implies the coordination situation of Mo atoms in CoMoP. The geometric position of Mo was also tested by extended EXAFS spectra relative to Mo foil and MoP, where the Mo R-space peaks (0.79, 1.48, and 2.22 Å) are attributed to Mo-O, MoP, and Mo-Co shells in CoMoP, respectively (Fig. 2h). The appearance of Mo-O in the first shell is caused by surface oxidation of the sample, which match the results of XPS.

The coordination center position of the Co atom decreases to 1.64 Å after Mo embedding (Fig. S4c), suggesting Co-P bond length is shortened, which may be due to structural distortion caused by Mo-embedding. Additionally, its intensity is slightly decreased compared to CoP and MoP (Figs. 2h, S4c), which indicates Mo and Co in CoMoP possess the lower coordination number, suggesting that Mo incorporation will lead to CoP lattice distortion. Subsequently, the wavelet transform was tested to explore the coordination situation. Fig. 2i show the Mo-O, Mo-P, and Mo-Co scattering path are corresponded to [4.74,0.79], [8.68,1.48] and [11.56,2.22], respectively in the k and R spaces. Collectively, these results indicate that the Mo-embedding CoP lattice leads to a higher oxidation state for Co and Mo. To elucidate the effect of surface oxygen on the catalyst structure, the CoMoP was exposed to air for oxidation 14 days and being tested compared with the bare-CoMoP. The XRD pattern show that the diffraction peaks of the

oxidation catalyst exposed to air are almost equivalent to that of the bare catalyst (Fig. S5), which confirms that surface oxygen does not alter the phase structure of the catalyst. The XPS results indicate that the binding energies of Co 2p, Mo 3d, P 2p, and O1s of the samples before and after exposure to air oxidation do not shift, confirming that surface oxygen does not alter the structure of the catalyst (Fig. S6). Meanwhile, the results of surface element content indicate that the content of Co, Mo, P, and O in the samples before and after exposure to air oxidation remains almost unchanged, further confirming that surface oxygen does not affect the structure of the catalyst (Table S3).

3.2. Performance analysis of electrocatalytic HMFOR and HER

The oxygen evolution reaction (OER) and HMFOR performances of CoP and CoMoP are studied in 1 M KOH. The OER process shows that the CoMoP, CoP, and nickel foam possess 1.37, 1.48, and 1.64 V initial potential (η_{onset}), respectively (Fig. S7). When HMF (100 mM) is added to the electrolyte, the η_{onset} of CoMoP is further reduced to 1.03 V (Fig. 3a), demonstrating that HMFOR is more favorable than OER while saving energy for hydrogen evolution. Fig. 3b shows the polarization curve of the catalysts for HMF oxidation activity. The results show that CoMoP have good performance may be due to Mo incorporation alters
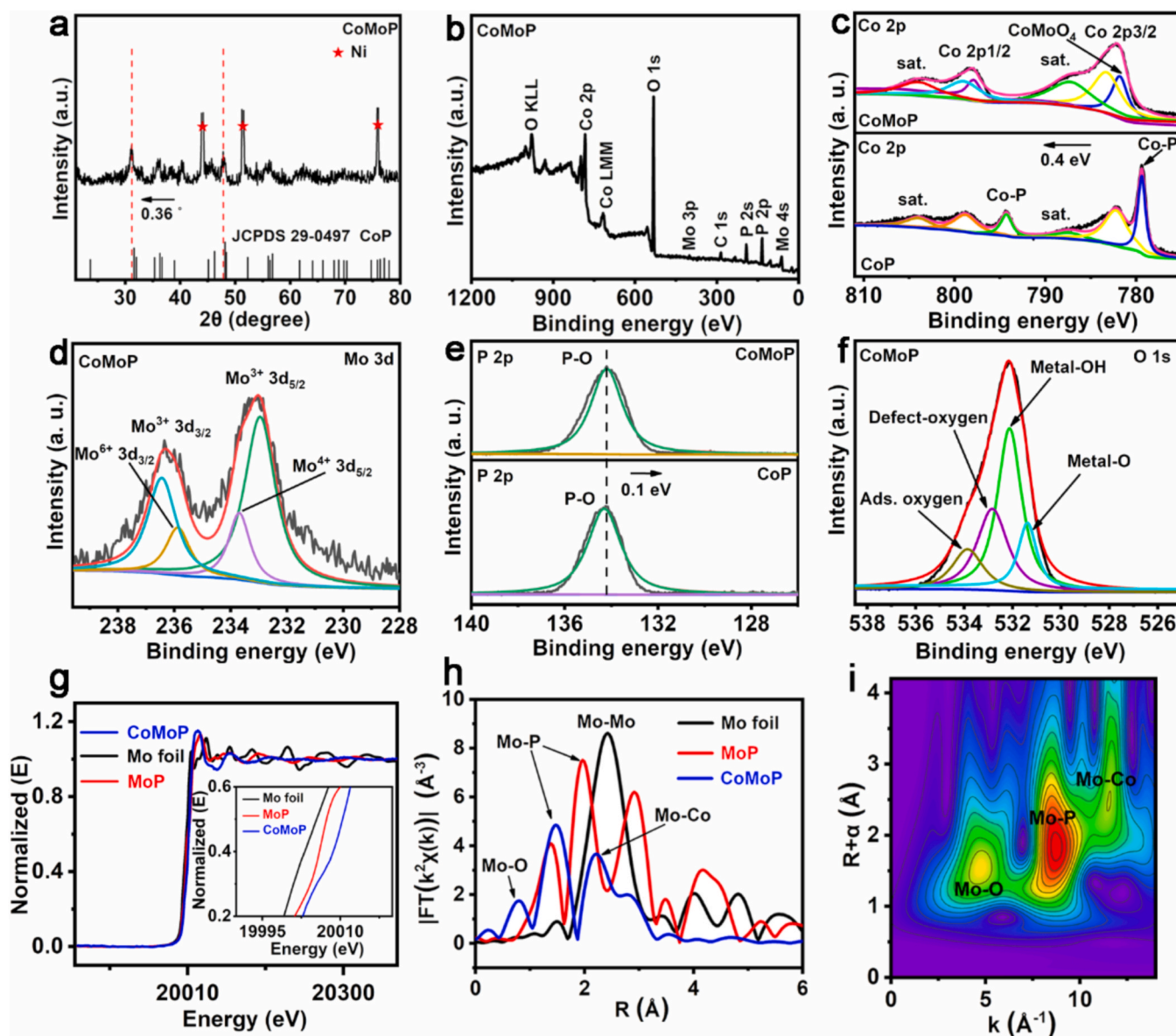
Fig. 2. (a) XRD patterns, and (b) full XPS spectra of CoMoP. The XPS spectra of (c) Co 2p, (d) Mo 3d, (e) P 2p, and (f) O 1s of CoMoP. XANES spectra at the (g) Mo K-edge, (h) FT of the Mo K-edge EXAFS of samples. (i) Wavelet transform of the Mo K-edge for CoMoP.

catalyst electronic structure and affects the HMFOR activity. Furthermore, the HMFOR activity of CoMoP surpass previous samples (Table S4). Notably, the CoP linear sweep voltammetry (LSV) curve shows that the anodic current first increases and drop afterward but again exhibit a sharp increase from 1.33 V, while the CoMoP-LSV plot sharply increases at 1.05 V. This may suggest that the two catalysts have different oxidation mechanisms for HMF and intermediate products. Our previous research shows that the possible intermediate products are 5-hydroxymethyl-2-furan carboxylic acid （HMFCA） and 2-formyl-5-furancarboxylic acid (FFCA) in HMFOR [48,49]. Therefore, CoMoP and CoP conducted electrochemical oxidation studies for HMFCA containing hydroxyl groups and FFCA containing formyl groups to clarify the correlation between catalysts and formyl/hydroxyl oxidation. Fig. S8a, c shows the η_{onset} of HMFCA and FFCA are 1.03 V and 1.04 V, respectively, which are lower than that of OER (1.38 V, 1.37 V), and the current density rises dramatically with the voltage. Therefore, it can be concluded that CoMoP can oxidize HMFCA and FFCA. Fig. S8b shows that the η_{onset} of HMFCA is 1.29 V, and the current density increases slowly with voltage, ultimately coinciding with the OER curve,

indicating that CoP possesses weak oxidation ability on HMFCA. When the voltage exceeds 1.29 V, a notable catalytic current is observed in FFCA oxidation (Fig. S8d). The above results imply that CoP can oxidize formyl groups but has a weak oxidation ability towards hydroxyl groups, while CoMoP has a strong oxidation ability towards both formyl and hydroxyl groups. Evaluate the intrinsic catalytic activity of CoMoP by testing the performance of different concentrations of HMF (Fig. 3c). This result suggests that the anodic current density rises with reactant concentration, indicating that CoMoP possess a high HMFOR intrinsic activity. Fig. 3d shows that the polarization curve displays very little change before and after ten conversions of HMF, exhibiting CoMoP excellent stability for HMFOR.

HER, as a cathodic reaction, is still crucial for the electrolytic cell system. CoMoP displays superior HER performance (Figs. 3e, S9) relative to CoP and Ni foam, implying the indispensability of Mo incorporation. The CoMoP HER property is also better than the previous catalysts (Table S5). To prove CoMoP true catalytic activity, its polarization curves without IR compensation are tested. The results show that the overpotential of the without IR compensation curve at 10 mA cm^{-2}
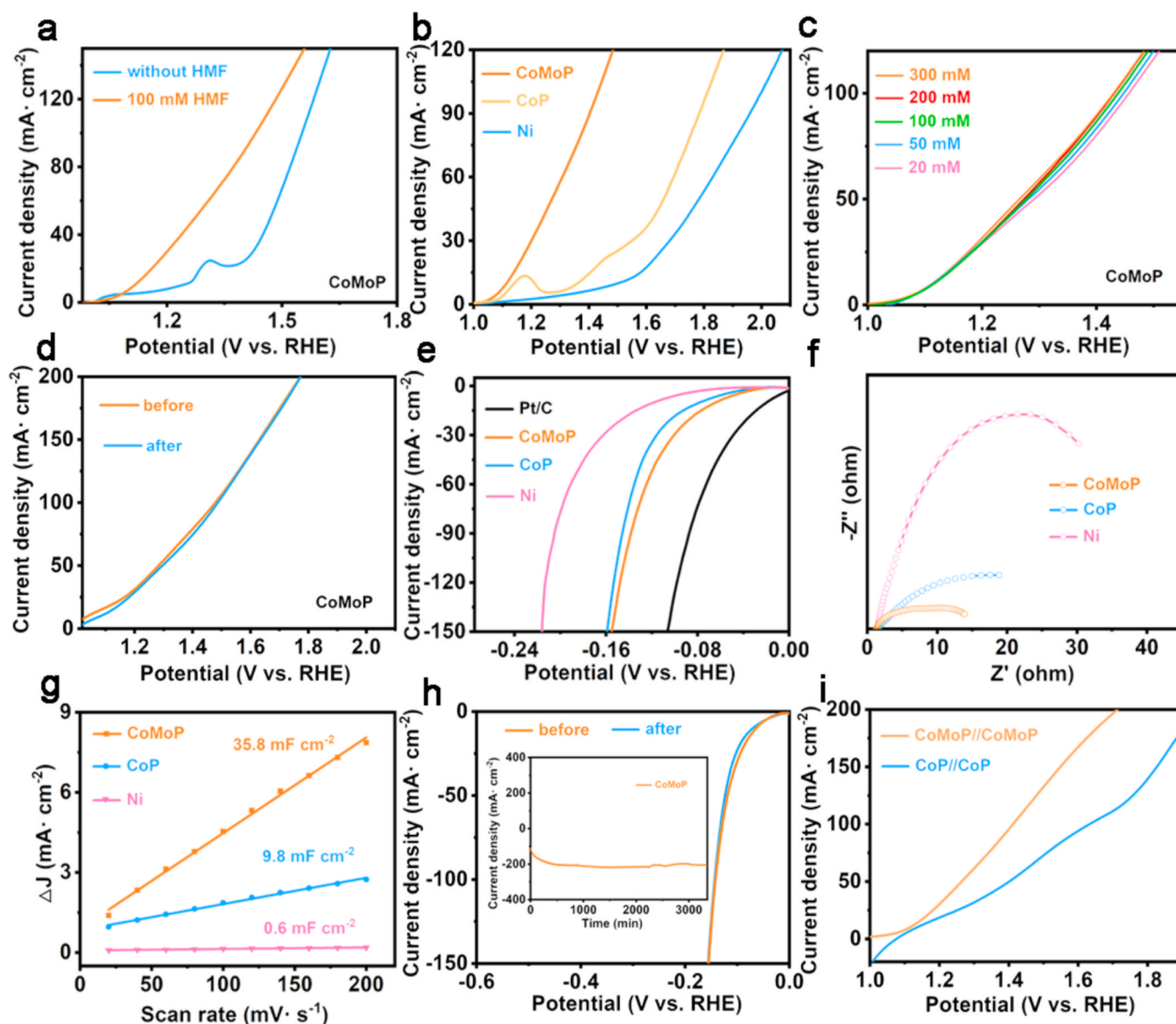
Fig. 3. (a,b) Polarization curves of CoMoP, CoP, and Ni foam. (c) Polarization curves for different concentrations and (d) CoMoP before and after 10 times HMFOR. (e) HER polarization curves for CoMoP, CoP, and Ni foam. (f) Nyquist plots and (g) capacitive currents density of CoMoP, CoP, and Ni foam. (h) Polarization curves for CoMoP before and after 20,000 cycles (Inset: I-t curve of CoMoP for 55 h). (i) Polarization curves for CoMoP and CoP coupling electrodes.

was greater than that of IR compensation (Fig. S10), which confirmed the necessity of IR compensation to eliminate the Ohmic voltage drop, thereby obtaining the true reaction activity of the CoMoP. The HER and HMFOR performance data normalized by ECSA values show that CoMoP has poorer activity than CoP and Ni foam (Fig. S11). This is due to CoMoP possess larger ECSA relative to CoP and Ni foam. The polarization curves of HER and HMFOR indicate that the performance of the sample remains almost unchanged before and after exposure to air oxidation, indicating that the surface oxygen of the catalyst does not affect the test results (Fig. S12). Fig. 3f shows the CoMoP possess a smaller impedance than that of CoP and Ni foam, indicating molybdenum incorporation contributes to enhance charge transfer kinetics. Meanwhile, the equivalent circuit model is given corresponding to the Nernst plot (Fig S13). The R_S, C_{PE}, and Rct are the electrolyte resistance between the reference electrode and the working electrode, double layer capacitance, and CoMoP resistance, respectively. The double-layer capacitance (C_{dl}) was utilized to measure electrochemical active surface area (ECSA) (Fig. S14). CoMoP possesses a larger C_{dl} (35.8 mF cm^{-2}) compared with CoP (9.8 mF cm^{-2}) and Ni foam (0.6 mF cm^{-2})

(Fig. 3g). The ECSA value are 1022.8 (CoMoP), 280 (CoP), and 17.1(Ni foam), respectively, illustrating appropriate Mo incorporation will bring more active sites, which is conducive to good HER performance. The catalysts intrinsic catalytic activity is investigated by measuring turnover frequency (TOF) and exchange current density (j_0). CoMoP have a larger TOF value (5.38 s^{-1} with 100 mV) in alkaline solution relative to CoP (2.19 s^{-1}) and Ni foam (1.37 s^{-1}) (Fig. S15), which implies the CoMoP has better intrinsic catalytic activity than CoP and Ni foam. Meanwhile, the j_0 of CoMoP is superior to CoP and Ni foam (Table S6), indicating CoMoP possess better conductivity than CoP and Ni foam. The results indicate the Mo introduction render CoP surface occur significant changes. The stability of CoMoP was tested.

through cyclic voltammetry and I-T curve. The performance curve shows a negligible reduction after 20,000 CV cycles (Fig. 3h). Furthermore, I-t curve of CoMoP displays a small current density loss after a constant voltage reaction 55 h (Fig. 3h inset). Fig. 3i shows that the electrolyzer (containing 100 mM HMF) voltage of CoMoP as anode and cathode is 1.41 V with 100 mA cm^{-2}, which is better relative to CoP (1.63 V), confirming CoMoP electrode has good coupling effect. CoMoP

possesses negligible composition (Fig. S16a) and structure change (Fig. S16b,c) after HER electrocatalysis, proving the catalyst have no occur surface reconstruction during hydrogen evolution reaction, which further confirm that high HER activity is due to Mo introduction.

To confirm the good HMFOR activity of CoMoP, the HMF adsorption state on the CoMoP surface was obtained before and after HMFOR. The used CoMoP exhibits greater infrared adsorption strength compare with bare CoMoP for carbonyl and hydroxyl groups (Fig. 4a), which confirming the used CoMoP surface is more beneficial to adsorb reactants. Thus, we suspect that the CoP electronic structure is regulated by Mo incorporation during HMFOR, leading to the essential change of the surface structure, making it easier adsorb reactant. (Fig. 4b). The in-situ Raman characterization is used to reveal structural changes of catalyst. Fig. 4c shows no stretching vibration peak under low applied voltage,

while the stretching vibration peak (931 cm^{-1}) at 0.5 V is attributed to the Mo-O species [35,50–52]. When the applied voltage increases to 0.7 V, the Raman peaks (662 cm^{-1}, 505 cm^{-1}) of β-CoOOH [53] and the stretching vibration (464 cm^{-1}) peak of Co-O appear [54]. The Raman peak intensity of β-CoOOH and Mo-O increases with potential, implying that CoMoP catalytic activity is optimized because β-CoOOH and Mo-O can promote the electrocatalytic activity in an alkaline medium [55,56]. To confirm that Mo incorporation can make CoMoP more easily form CoOOH and Mo-O, the CoP in-situ Raman characterization is tested. The results show that CoP only exhibits a weak stretching vibration Co-O peak at 0.5 V voltage, indicating the Mo incorporation can enhance CoMoP surface reconstruction and HMFOR (Fig. 4d). TEM characterization indicates that CoOOH, MoO₃, and CoO is formed on the CoMoP surface after HMFOR (Fig. 4e, f, g), which confirms the formation of
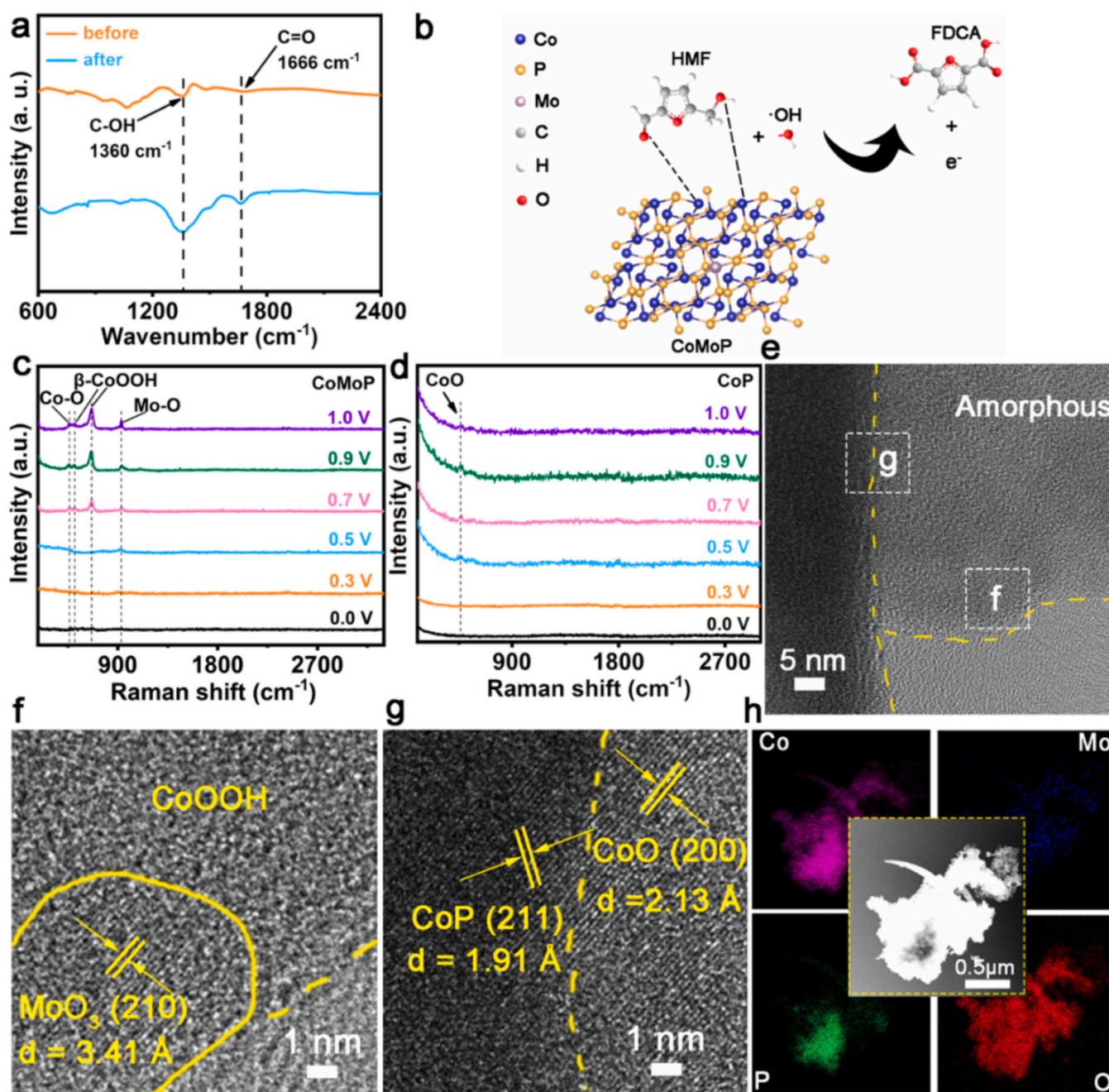

Fig. 4. (a) Adsorption infrared spectra of HMF on CoMoP before and after HMFOR. (b) The mechanism of HMFOR. In-situ Raman spectra of prepared (c) CoMoP and (d) CoP. (e-g) HRTEM image of CoMoP after HMFOR. (h) TEM image and the corresponding elemental mapping images of CoMoP after HMFOR.

CoOOH and Mo-O and Co-O species on the CoMoP surface during HMFOR. Meanwhile, the oxygen content of the catalyst increases correspondingly before the reaction in TEM mapping (Fig. 4h, Table S7). To further confirm this conclusion, the XRD was used to test CoMoP after HMFOR. The results indicate the emergence of new diffraction peaks ($2\theta = 14.5°$ and $36.5°$) are attributed to MoO_3 and CoO species (Fig. S17), respectively, which further confirms the catalyst surface structure is changed during HMFOR. Additionally, the XPS spectra of the catalyst after HMFOR are tested as compared. The relative intensity of the peaks attributed to Co oxides (Fig. S18a) and Mo oxides (Fig. S18b) significantly increases after HMFOR. Meanwhile, the intensity of the P 2p peak decreases relative to before the reaction (Fig. S18c) due to a layer of oxidation species are reconstructed on the CoMoP surface. Besides, O XPS spectra show a significant increase in peak intensity belonging to the defected oxygen (Fig. S18d), and the peak position of Mo 3d shifted negatively by 0.9 eV compared to before the reaction (Fig. S18b), indicating that the O-defects proportion in catalyst are raised during reaction. As a result, O-defects may be filled by OH·in alkaline media, and the low oxidation state cation will be excessively oxidized to the high valence state species and enhance HMFOR.

3.3. Kinetic analysis and technology optimization

HMF, FDCA, and other products obtained at 1.36 V constant voltage were monitored via high-performance liquid chromatography (Figs. S19, S20). Fig. S21 shows that HMF is gradually consumed and FDCA accumulates as the charge.

increases, while HMF is entirely transformed after passing 596 C charge at 1.36 V constant voltage (Fig. S22). 2,5-diformylfuran (DFF) was not discovered during HMFOR. Hence, HMF may be converted into FDCA by preferential oxidation of aldehyde groups (Fig. 5a). Here, it is assumed that the HMF oxidation reaction is first-order, and the value of k_2 is the smallest among the rate coefficients (k_1-k_3) (Fig. S23). Therefore, the oxidation of 5-hydroxymethyl-2-furan carboxylic acid (HMFCA) to FFCA is considered a decisive step for HMFOR. Fig. 5b exhibits the variation of reactant and product with charge for CoMoP. As a comparison, we tested the variation of reactant and product with charge for CoP (Fig. S24). The results show that it is difficult for CoP to completely oxidize HMFCA with the same charge, which further confirm that Mo-O and CoOOH on the CoMoP surface during HMFOR are active centers for hydroxyl oxidation. As is well known, atom doping strategies is usually employed to improve the catalytic performance and tune catalyst d-electron [57]. Utilizing Mo incorporation CoP filling Co d-orbitals and regulate the d electrons of CoMoP, which increasing electron transfer rate of catalyst. This makes CoOOH and MoO_3 are formed on the CoMoP surface during the HMFOR process, enhancing the adsorption behavior of HMF [41] and promoting HMFOR activity. This is consistent with in situ Raman, infrared, and impedance results. As shown in Fig. 5c and Table S8, CoMoP has good HMFOR performance relative to CoP and Ni foam. Employing infrared spectroscopy to track the HMFOR process further reveals the rate-limiting step. The result suggests that HMF (1078 cm^{-1}) and 5-formyl furan-2-carboxylic acid (FFCA) (790 cm^{-1}) infrared peaks increasingly disappear during HMFOR, but HMFCA infrared peak (831 cm^{-1}) is remained (Fig. 5d). Meanwhile, FDCA infrared peak (809 cm^{-1}) increasingly increase with reaction. Therefore, the HMFCA to FFCA reaction rate is lower relative to HMF to HMFCA and FFCA to FDCA, suggesting that the HMFCA conversion to FFCA is the rate-determining. Fig. S25 shows the catalyst stability is obtained by testing I-T curve (10 times). Fig. 5e shows that the CoMoP still maintains good performance after five times oxidation reaction. To investigate the effects of CoMoP on the Faraday efficiency and selectivity of HMFOR under different oxidation potentials, we selected potentials of 1.30 V, 1.42 V, and 1.48 V for the oxidation reaction of HMF in the full cell. The results show that the HMF conversion rate and FDCA selectivity slightly decrease at 1.3 V oxidation potential compared to high oxidation potential, while the HMF conversion rate

and FDCA selectivity remained almost unchanged at high oxidation potential (1.42 V, 1.48 V) (Fig. S26). This may be due to the longer oxidation time required to convert HMF and HMFCA into FDCA at low oxidation potentials. Meanwhile, the Faraday efficiency remains almost unchanged at different oxidation potentials, confirming that different oxidation potentials do not alter the actual efficiency of HMFOR. To verify the effectiveness of the two electrodes coupling system (CoMoP//CoMoP) at 1.36 V, the relational testing was conducted. For HER, we can clearly see that opulent H_2 bubbles are fleetly released from the electrodes (Fig. S27a). For HMFOR, the results show that the HMF is entirely transformed after passing 583.5 C charge at 1.36 V with CoMoP//CoMoP (Fig. S27b,c). The HMF conversion rate, FDCA selectivity, and Faraday efficiency are 97.5%, 96.5%, and 93.3%, respectively (Fig. S27d). In HMFOR, the diffusion of electrolytes plays a crucial role in the reaction rate. Thus, CoMoP is coupled with a flow-by-type flow reactor (fabricated by a 3D printer) to weaken the concentration polarization effect (Fig. 5f). Fig. 5g shows that the flow reactor exhibits good performance at 0.2 mL/min and decreases with increasing flow rate. Meanwhile, CoMoP possess good catalytic stability in a flow reactor connected to a 1.5 V DC power (Figs. 5h, S28). To further optimize the reaction technology, finite element simulation was used to analyze the content of HMF and FDCA. Most of HMF (100 mM) (Fig. 5i) has already been consumed, and almost completely convert to FDAC (100 mM) (Fig. 5j) by three reaction modules.

3.4. DFT calculations and mechanism inference

To investigate the effect of Mo incorporation on HER and HMFOR, density functional theory (DFT) calculations were performed. For HER, CoP (Fig. 6a) and CoMoP (Fig. 6b) with H adsorption theoretical models were established. Fig. 6c shows that CoP and CoMoP with H adsorption compare with Fermi level raise −2.02 to −1.63 eV, demonstrating d-band center upshift after Mo incorporation. Meanwhile, Mo incorporation can raise the antibonding level and enhance the interaction between adsorbate and surface. The above results show that the d-band center raise and fewer electrons filled in antibonding states after adding Mo increases hydrogen adsorption. To further confirm the superiority of CoMoP over HER, investigate the effect of Mo on hydrogen-free energy. CoMoP possesses a much smaller $|\Delta G_{H^*}|$ than that of CoP (Fig. 6d and Table S9), indicating that CoMoP has highly active for HER. This result is consistent with the XPS analysis because the high electron density induce by Mo doping at the P-site is conducive to the adsorption of more hydrogen protons. For HMFOR, adsorption models of HMF on CoP (Fig. 6e) and CoMoP (Fig. 6f) surfaces.

were constructed to obtain HMF adsorption energy. Fig. 6g shows that CoMoP has larger density of state (DOS) compare with CoP, implying that CoMoP structure conducive to electron conduction. Additionally, the DOS data match the XANES results where Mo changes the electronic structure of the catalyst. Fig. 6h shows that CoMoP has 1.98 eV HMF adsorption energy, while CoP only is 1.12 eV, implying that Mo incorporation can promote HMFOR kinetics. For the HER in alkaline solution, the water adsorption and the adsorption/desorption of various intermediates are the key descriptors. Therefore, the water adsorbed energy (E_{H_2O}) on CoP and CoMoP were calculated. Meanwhile, the free-energy change of the HER process from H_2O to H_2 are calculated (Figs. S29, S30). The larger E_{H_2O} of CoMoP (−0.479 eV) than that of CoP (−0.375 eV) implies that Mo incorporation increases the effective water adsorption (Fig. S31). As for the favorable pathways on each of catalysts in alkaline conditions, CoMoP is significantly superior to the CoP (Fig. S32a). The above results suggest that Mo incorporation optimizes the CoMoP d-band center and changes of free-energy changes to promote the HER process. Due to the CoMoP surface reconstruct as CoOOH and MoO_3 during the HMFOR, thus DFT model of CoMoP-CoOOH and CoMoP-MoO_3 adsorb HMF are established to reveal the true reaction active site of the catalyst in HMFOR (Fig. S32b,c). The result show that the adsorption energy is CoMoP-CoOOH > CoMoP-MoO_3 and superior to
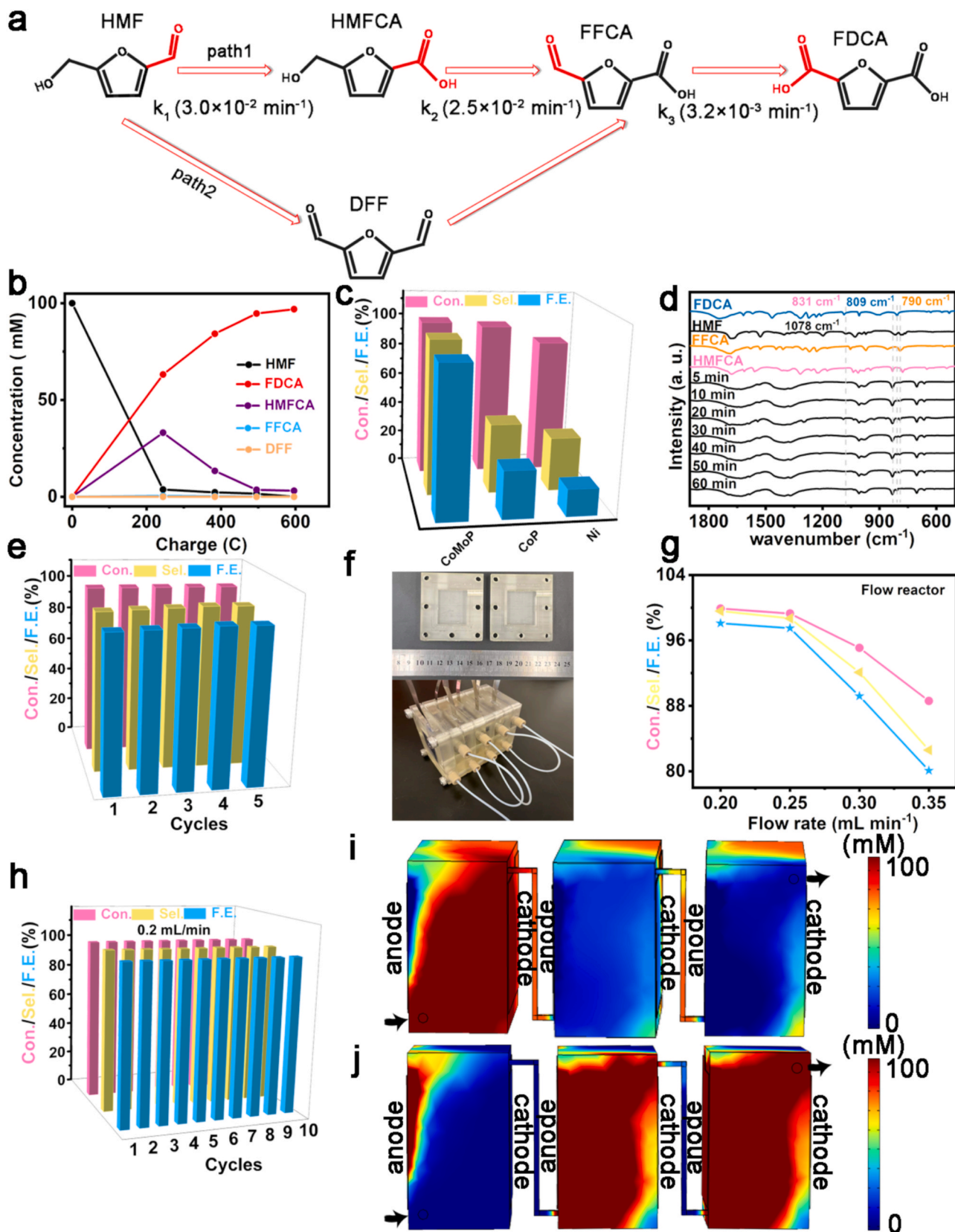
Fig. 5. (a) The oxidation path and kinetic constant of HMF for CoMoP. (b) Concentration curves with the reaction for HMF, FDCA, HMFCA, FFCA, and DFF during the HMFOR. (c) HMF conversion, FDCA selectivity, and Faraday efficiency of CoMoP, CoP, and Ni foam. (d) Infrared tracking spectra with different HMFOR time. (e) The HMFOR of CoMoP at five successive cycles. (f) 3D printing components of flow reactors. (g) HMF conversion, FDCA selectivity, and FE at different flow rates in a flow reactor. (h) The HMFOR of the flow reactor at ten successive cycles. (i) The numerical simulation of the HMF and (j) FDCA concentration distribution in the flow-by reactor (arrows: the direction of flow).
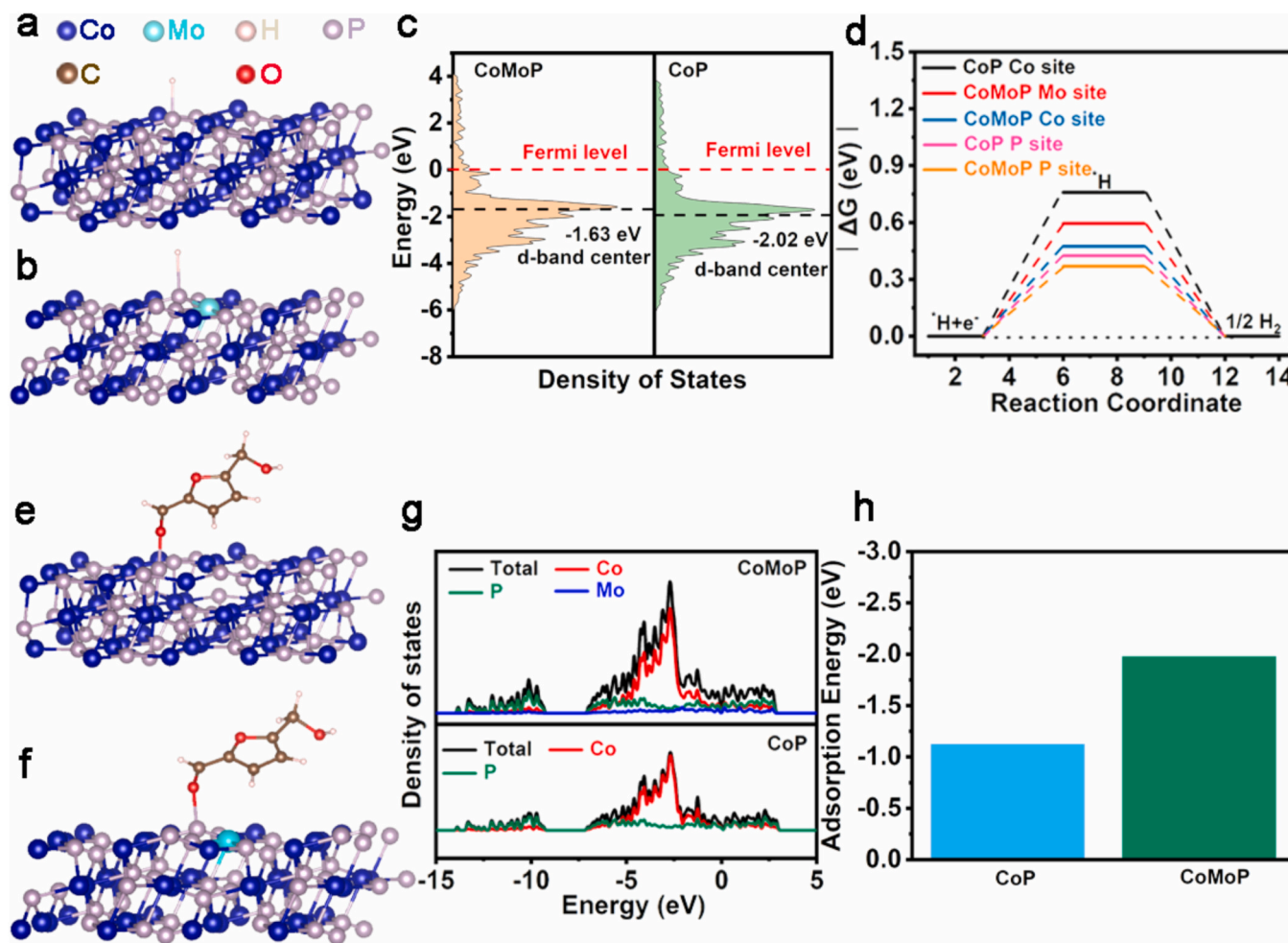
Fig. 6. Theoretical models of CoP (a) and CoMoP (b) adsorption H. (c) DOS of CoMoP and CoP with adsorption hydrogen. (d) Free energy diagram of CoMoP and CoP with various sites for HER. Theoretical models of CoP (e) and CoMoP (f) adsorption HMF. (g) DOS of CoMoP and CoP with adsorption HMF and (h) HMF adsorption energy.

CoMoP and CoP (Fig. S32d), which further confirm that the reconstruct phases (CoOOH, MoO₃) are active species for HMF oxidation. DFT data match the surface adsorption infrared data of the samples (Fig. 4a), which further verifying the catalytic mechanism for catalyst surface adsorption HMF (Fig. 4b). On the basis of the above analyses, the HMFOR mechanism over MoO₃-CoMoP-CoOOH was proposed (Fig. S33). Nucleophilic HMF molecules with conjugated C=C groups were selectively adsorbed or bound over the MoO₃-CoMoP-CoOOH, and then reacted with the in-situ formed electrophilic OH_{ads} species. Afterwards, oxidation of the hydroxyl and aldehyde groups of HMF molecules to give corresponding HMFCA and FFCA intermediates, FDCA product, and H_2O.

4. Conclusion

In conclusion, we incorporated Mo into CoP to induce lattice expansion to enhance HER and HMFOR. DFT theoretical calculation confirms that Mo incorporation can raise Co d-band center, which induces more H adsorption on phosphorus sites of CoMoP to enhance HER activity. Adsorption infrared and DFT data suggest that Mo incorporation can enhance HMF adsorption on the CoMoP surface. In situ Raman spectroelectrochemistry and XPS demonstrate that the CoOOH, Co-O, and Mo-O species are generated more easily on the CoMoP surface. It is because incorporation of Mo lead to abundant oxygen defects on

CoMoP surface, and the OH·can fill defect-sites, thus promoting the oxidation of low-valence metal ions to obtain high oxidation state species synergistic catalysis HMF. Meanwhile, the Mo-O and CoOOH species of surface reconstruction were identified as the active center for the initial oxidation of hydroxyl, which provided an effective strategy for the d-electron complementation principle to adjust the electronic structure of the catalyst to improve the activities of HER and HMFOR.

CRediT authorship contribution statement

Honglei Wang: Conceptualization, Methodology, Validation, Data curation, Formal analysis, Writing – original draft, Writing – review & editing. **Caiyun Niu:** Conceptualization, Methodology, Validation, Data curation, Formal analysis. **Wen Liu:** Methodology, Validation, Data curation, Formal analysis. **Shengyang Tao:** Conceptualization, Resources, Formal analysis, Supervision, Project administration, Funding acquisition, Writing – review & editing.

Declaration of Competing Interest

We declare that we have no known competing financial interests or personal relationships that could have appeared to influence the work reported in this paper.

Data availability

Data will be made available on request.

Acknowledgments

Appendix A. Supporting information

Supplementary data associated with this article can be found in the online version at doi:10.1016/j.apcatb.2023.123249.

References

[1] B. You, Y. Sun, Innovative strategies for electrocatalytic water splitting, Acc. Chem. Res. 51 (2018) 1571–1580.

[2] N.S. Lewis, D.G. Nocera, Powering the planet: chemical challenges in solar energy utilization, Proc. Natl. Acad. Sci. USA 103 (2006) 15729–15735.

[3] R.J. van Putten, J.C. van der Waal, E. de Jong, C.B. Rasrendra, H.J. Heeres, J.G. de Vries, Hydroxymethylfurfural, a versatile platform chemical made from renewable resources, Chem. Rev. 113 (2013) 1499–1597.

[4] S.V. Amar, K. Mohanty, Jean-Mathieu Pin, Manjusri Misra, Composites from renewable and sustainable resources: challenges and innovations, Science 36 (2018) 536–542.

[5] R. Zhang, S. Jiang, Y. Rao, S. Chen, Q. Yue, Y. Kang, Electrochemical biomass upgrading on CoOOH nanosheets in a hybrid water electrolyzer, Green Chem. 23 (2021) 2525–2530.

[6] H. Liu, W. Jia, X. Yu, X. Tang, X. Zeng, Y. Sun, T. Lei, H. Fang, T. Li, L. Lin, Vitamin C-assisted synthesized Mn-Co oxides with improved oxygen vacancy concentration: boosting lattice oxygen activity for the air-oxidation of 5-(hydroxymethyl)furfural, ACS Catal. 11 (2021) 7828–7844.

[7] G. Zhao, G. Hai, P. Zhou, Z. Liu, Y. Zhang, B. Peng, W. Xia, X. Huang, G. Wang, Electrochemical oxidation of 5–hydroxymethylfurfural on CeO_2-modified Co_3O_4 with regulated intermediate adsorption and promoted charge transfer, Adv. Funct. Mater. 33 (2023), 2213170.

[8] C. Xu, E. Paone, D. Rodriguez-Padron, R. Luque, F. Mauriello, Recent catalytic routes for the preparation and the upgrading of biomass derived furfural and 5-hydroxymethylfurfural, Chem. Soc. Rev. 49 (2020) 4273–4306.

[9] W. Guo, H.J. Heeres, J. Yue, Continuous synthesis of 5-hydroxymethylfurfural from glucose using a combination of $AlCl_3$ and HCl as catalyst in a biphasic slug flow capillary microreactor, Chem. Eng. J. 381 (2020) 122754.

[10] E. Hayashi, Y. Yamaguchi, K. Kamata, N. Tsunoda, Y. Kumagai, F. Oba, M. Hara, Effect of MnO_2 crystal structure on aerobic oxidation of 5-hydroxymethylfurfural to 2,5-furandicarboxylic acid, J. Am. Chem. Soc. 141 (2019) 890–900.

[11] M. Kim, Y. Su, A. Fukuoka, E.J.M. Hensen, K. Nakajima, Aerobic oxidation of 5-(Hydroxymethyl)furfural cyclic acetal enables selective furan-2,5-dicarboxylic acid formation with CeO_2-supported gold catalyst, Angew. Chem. Int. Ed. 57 (2018) 8235–8239.

[12] Y.T. Liao, V.C. Nguyen, N. Ishiguro, A.P. Young, C.K. Tsung, K.C.W. Wu, Engineering a homogeneous alloy-oxide interface derived from metal-organic frameworks for selective oxidation of 5-hydroxymethylfurfural to 2,5-furandicarboxylic acid, Appl. Catal. B 270 (2020), 118805.

[13] N. Zhang, Y. Zou, L. Tao, W. Chen, L. Zhou, Z. Liu, B. Zhou, G. Huang, H. Lin, S. Wang, Electrochemical oxidation of 5-Hydroxymethylfurfural on nickel nitride/carbon nanosheets: reaction pathway determined by in situ sum frequency generation vibrational spectroscopy, Angew. Chem. Int. Ed. 58 (2019) 15895–15903.

[14] L. Guo, X. Zhang, L. Gan, L. Pan, C. Shi, Z.F. Huang, X. Zhang, J.J. Zou, Advances in selective electrochemical oxidation of 5-Hydroxymethylfurfural to produce high-value chemicals, Adv. Sci. 10 (2023), 2205540.

[15] Y. Lu, C.L. Dong, Y.C. Huang, Y. Zou, Z. Liu, Y. Liu, Y. Li, N. He, J. Shi, S. Wang, Identifying the geometric site dependence of spinel oxides for the electrooxidation of 5-hydroxymethylfurfural, Angew. Chem. Int. Ed. 59 (2020) 19215–19221.

[16] X. Deng, G.Y. Xu, Y.J. Zhang, L. Wang, J. Zhang, J.F. Li, X.Z. Fu, J.L. Luo, Understanding the roles of electrogenerated Co^{3+} and Co^{4+} in selectivity-tuned 5-hydroxymethylfurfural oxidation, Angew. Chem. Int. Ed. 60 (2021) 20535–20542.

[17] P.W. Menezes, S. Yao, R. Beltran-Suito, J.N. Hausmann, P.V. Menezes, M. Driess, Facile access to an active gamma-NiOOH electrocatalyst for durable water oxidation derived from an intermetallic nickel germanide precursor, Angew. Chem. Int. Ed. 60 (2021) 4640–4647.

[18] Y. Song, W. Xie, Y. Song, H. Li, S. Li, S. Jiang, J.Y. Lee, M. Shao, Bifunctional integrated electrode for high-efficient hydrogen production coupled with 5-hydroxymethylfurfural oxidation, Appl. Catal. B 312 (2022), 121400.

[19] Q. Qian, J. Zhang, J. Li, Y. Li, X. Jin, Y. Zhu, Y. Liu, Z. Li, A. El-Harairy, C. Xiao, G. Zhang, Y. Xie, Artificial heterointerfaces achieve delicate reaction kinetics towards hydrogen evolution and hydrazine oxidation catalysis, Angew. Chem. Int. Ed. 60 (2021) 5984–5993.

[20] Y. Qiang, D. Ouyang, L. You, D. Liu, X. Zhao, Liquid flow fuel cell with an electrodeposition-modified nickel foam anode for efficient oxidation of 5-hydroxymethylfurfural to produce 2, 5-furandicarboxylic acid with co-generation of electricity, Chem. Eng. J. 469 (2023), 143832.

[21] Y. Lin, K. Sun, S. Liu, X. Chen, Y. Cheng, W.C. Cheong, Z. Chen, L. Zheng, J. Zhang, X. Li, Y. Pan, C. Chen, Construction of CoP/NiCoP nanotadpoles heterojunction interface for wide pH hydrogen evolution electrocatalysis and supercapacitor, Adv. Energy Mater. 9 (2019) 1901213.

[22] S. Li, S. Wang, Y. Wang, J. He, K. Li, Y. Xu, M. Wang, S. Zhao, X. Li, X. Zhong, J. Wang, Doped Mn enhanced NiS electrooxidation performance of HMF into FDCA at industrial-level current density, Adv. Funct. Mater. 33 (2023), 2214488.

[23] H. Wang, Y. Xie, H. Cao, Y. Li, L. Li, Z. Xu, X. Wang, N. Xiong, K. Pan, Flower-like nickel phosphide microballs assembled by nanoplates with exposed high-energy (0 0 1) facets: efficient electrocatalyst for the hydrogen evolution reaction, ChemSusChem 10 (2017) 4899–4908.

[24] T. Wei, W. Liu, S. Zhang, Q. Liu, J. Luo, X. Liu, A dual-functional Bi-doped Co_3O_4 nanosheet array towards high efficiency 5-hydroxymethylfurfural oxidation and hydrogen production, Chem. Commun. 59 (2023) 442–445.

[25] C. Liu, X.R. Shi, K. Yue, P. Wang, K. Zhan, X. Wang, B.Y. Xia, Y. Yan, S-species-evoked high-valence $Ni^{2+\delta}$ of the evolved β-$Ni(OH)_2$ electrode for selective oxidation of 5-Hydroxymethylfurfural, Adv. Mater. 35 (2023), 2211177.

[26] R. Zhang, Z. Wei, G. Ye, G. Chen, J. Miao, X. Zhou, X. Zhu, X. Cao, X. Sun, "d-electron complementation" induced V-Co phosphide for efficient overall water splitting, Adv. Energy Mater. 11 (2021), 2101758.

[27] C. Yang, C. Wang, L. Zhou, W. Duan, Y. Song, F. Zhang, Y. Zhen, J. Zhang, W. Bao, Y. Lu, D. Wang, F. Fu, Refining d-band center in $Ni_{0.85}Se$ by Mo doping: a strategy for boosting hydrogen generation via coupling electrocatalytic oxidation 5-hydroxymethylfurfural, Chem. Eng. J. 422 (2021), 130125.

[28] S. Chandrasekaran, R. Hu, L. Yao, L. Sui, Y. Liu, A. Abdelkader, Y. Li, X. Ren, L. Deng, Mutual self-regulation of d-Electrons of single atoms and adjacent nanoparticles for bifunctional oxygen electrocatalysis and rechargeable zinc-air batteries, Nano-Micro Lett. 15 (2023) 48–66.

[29] M.M. Jaksic, Advances in electrocatalysis for hydrogen evolution in the light of the brewer-engel valence-bond theory, J. Mol. Catal. 38 (1986) 161–202.

[30] H. Yan, Y. Xie, A. Wu, Z. Cai, L. Wang, C. Tian, X. Zhang, H. Fu, Anion-modulated HER and OER activities of 3D Ni-V-based interstitial compound heterojunctions for high-efficiency and stable overall water splitting, Adv. Mater. 31 (2019), 1901174.

[31] C.C.L. McCrory, S. Jung, J.C. Peters, T.F. Jaramillo, Benchmarking heterogeneous electrocatalysts for the oxygen evolution reaction, J. Am. Chem. Soc. 135 (2013) 16977–16987.

[32] W. Lu, J. Shen, P. Zhang, Y. Zhong, Y. Hu, X.W.D. Lou, Construction of CoO/Co-Cu-S hierarchical tubular heterostructures for hybrid supercapacitors, Angew. Chem. Int. Ed. 58 (2019) 15441–15447.

[33] E. Cao, Z. Chen, H. Wu, P. Yu, Y. Wang, F. Xiao, S. Chen, S. Du, Y. Xie, Y. Wu, Z. Ren, Boron-induced electronic-structure reformation of CoP nanoparticles drives enhanced pH-universal hydrogen evolution, Angew. Chem. Int. Ed. 59 (2020) 4154–4160.

[34] Y.N. Zhou, W.H. Hu, Y.N. Zhen, B. Dong, Y.W. Dong, R.Y. Fan, B. Liu, D.P. Liu, Y. M. Chai, Metallic MoO layer promoting high-valence Mo doping into CoP nanowires with ultrahigh activity for hydrogen evolution at 2000 mA cm^{-2}, Appl. Catal. B 309 (2022), 121230.

[35] G. Yang, Y. Jiao, H. Yan, Y. Xie, A. Wu, X. Dong, D. Guo, C. Tian, H. Fu, Interfacial engineering of MoO_2-FeP heterojunction for highly efficient hydrogen evolution coupled with biomass electrooxidation, Adv. Mater. 32 (2020) 2000455.

[36] Y. Jin, H. Wang, J. Li, X. Yue, Y. Han, P.K. Shen, Y. Cui, Porous MoO_2 nanosheets as non-noble bifunctional electrocatalysts for overall water splitting, Adv. Mater. 28 (2016) 3785–3790.

[37] Y. Wang, P. Yang, Y. Gong, D. Liu, S. Liu, W. Xiao, Z. Xiao, Z. Li, Z. Wu, L. Wang, Amorphous high-valence Mo-doped NiFeP nanospheres as efficient electrocatalysts for overall water-splitting under large-current density, Chem. Eng. J. 468 (2023), 143833.

[38] Z. Pan, L. Jin, C. Yang, X. Ji, M. Liu, Mo-doped MnO_2@CC electrode for high-performance 2.4 V aqueous asymmetric supercapacitors, Chem. Eng. J. 470 (2023), 144084.

[39] K. Fan, Y. Ji, H. Zou, J. Zhang, B. Zhu, H. Chen, Q. Daniel, Y. Luo, J. Yu, L. Sun, Hollow iron-Vanadium composite spheres: a highly efficient iron-based water oxidation electrocatalyst without the need for nickel or cobalt, Angew. Chem. Int. Ed. 56 (2017) 3289–3293.

[40] X. Dong, H. Yan, Y. Jiao, D. Guo, A. Wu, G. Yang, X. Shi, C. Tian, H. Fu, 3D hierarchical V–Ni-based nitride heterostructure as a highly efficient pH-universal electrocatalyst for the hydrogen evolution reaction, J. Mater. Chem. A 7 (2019) 15823–15830.

[41] H. Wang, C. Li, J. An, Y. Zhuang, S. Tao, Surface reconstruction of NiCoP for enhanced biomass upgrading, J. Mater. Chem. A 9 (2021) 18421–18430.

[42] L. Deng, K. Zhang, D. Shi, S. Liu, D. Xu, Y. Shao, J. Shen, Y. Wu, X. Hao, Rational design of Schottky heterojunction with modulating surface electron density for high-performance overall water splitting, Appl. Catal. B 299 (2021), 120660.

[43] H. Wang, Y. Wang, J. Zhang, X. Liu, S. Tao, Electronic structure engineering through Fe-doping CoP enables hydrogen evolution coupled with electro-Fenton, Nano Energy 84 (2021) 105943.

[44] S. Zhao, C. Tan, C.T. He, P. An, F. Xie, S. Jiang, Y. Zhu, K.H. Wu, B. Zhang, H. Li, J. Zhang, Y. Chen, S. Liu, J. Dong, Z. Tang, Structural transformation of highly active metal–organic framework electrocatalysts during the oxygen evolution reaction, Nat. Energy 5 (2020) 881–890.

[45] C. Li, H. Jang, M.G. Kim, L. Hou, X. Liu, J. Cho, Ru-incorporated oxygen-vacancy-enriched MoO_2 electrocatalysts for hydrogen evolution reaction, Appl. Catal. B 307 (2022), 121204.

[46] X. Yu, J. Zhao, M. Johnsson, Interfacial engineering of nickel hydroxide on cobalt phosphide for alkaline water electrocatalysis, Adv. Funct. Mater. 31 (2021), 2101578.

[47] H. Wang, S. Tao, Fabrication of a porous NiFeP/Ni electrode for highly efficient hydrazine oxidation boosted H_2 evolution, Nanoscale Adv. 3 (2021) 2280–2286.

[48] H. Wang, J. Zhang, S. Tao, Nickel oxide nanoparticles with oxygen vacancies for boosting biomass-upgrading, Chem. Eng. J. 444 (2022), 136693.

[49] H. Wang, Y. Zhou, S. Tao, CoP-CoOOH heterojunction with modulating interfacial electronic structure: a robust biomass-upgrading electrocatalyst, Appl. Catal. B 315 (2022), 121588.

[50] N. Ke, H. Huang, F. Wang, A. Huang, C. Tan, B. Dong, Y. Wu, L. Hao, X. Xu, S. Agathopoulos, Self-supported MoO_2/$MoSi_2$ ceramic electrode for high current density hydrogen evolution reaction, ACS Sustain. Chem. Eng. 11 (2023) 3769–3779.

[51] Y. Jung, H. Ryu, H. Kim, D. Moon, J. Joo, S.C. Hong, J. Kim, G.H. Lee, Nucleation and growth of monolayer MoS_2 at multisteps of MoO_2 crystals by sulfurization, ACS Nano 17 (2023) 7865–7871.

[52] H. Zhang, Y. Wu, Z. Huang, X. Shen, B. Li, Z. Zhang, R. Wu, D. Wang, C. Yi, K. He, Y. Zhou, J. Liu, B. Li, X. Duan, Synthesis of two-dimensional MoO_2 nanoplates with large linear magnetoresistance and nonlinear hall effect, Nano Lett. 23 (2023) 2179–2186.

[53] P. Ji, X. Luo, D. Chen, H. Jin, Z. Pu, W. Zeng, J. He, H. Bai, Y. Liao, S. Mu, Significantly improved water oxidation of CoP catalysts by electrochemical activation, ACS Sustain. Chem. Eng. 8 (2020) 17851–17859.

[54] Y. Lyu, J. Zheng, Z. Xiao, S. Zhao, S.P. Jiang, S. Wang, Identifying the intrinsic relationship between the restructured oxide layer and oxygen evolution reaction performance on the cobalt pnictide catalyst, Small 16 (2020), 1906867.

[55] C. Luan, M. Corva, U. Hagemann, H. Wang, M. Heidelmann, K. Tschulik, T. Li, Atomic-scale insights into morphological, structural, and compositional evolution of CoOOH during oxygen evolution reaction, ACS Catal. 13 (2023) 1400–1411.

[56] G. Wei, C. Wang, X. Zhao, S. Wang, F. Kong, Plasma-assisted synthesis of Ni_4Mo/MoO_2@carbon nanotubes with multiphase-interface for high-performance overall water splitting electrocatalysis, J. Alloy. Compd. 939 (2023), 168755.

[57] H. Tabassum, R. Zou, A. Mahmood, Z. Liang, Q. Wang, H. Zhang, S. Gao, C. Qu, W. Guo, S. Guo, A universal strategy for hollow metal oxide nanoparticles encapsulated into B/N Co-doped graphitic nanotubes as high-performance lithium-ion battery anodes, Adv. Mater. 30 (2018), 1705441.